

Defect detection and imaging using electromagnetic acoustic transducer with butterfly coil

Cite as: Rev. Sci. Instrum. 95, 064704 (2024); doi: 10.1063/5.0198404

Submitted: 18 January 2024 • Accepted: 20 May 2024 •

Published Online: 4 June 2024



View Online



Export Citation



CrossMark

Chaoqun Wang, Jian Ma, Xue Bai, and Jianwei Chen

AFFILIATIONS

Laser Institute, Qilu University of Technology (Shandong Academy of Sciences), 250104 Jinan, China

^aAuthor to whom correspondence should be addressed: mj@sdlaser.cn

ABSTRACT

Electromagnetic ultrasonic detection technology utilizes the electromagnetic coupling method to generate and receive ultrasonic waves without a couplant, which is suitable for rapid detection. However, the detection can be affected by the spatial distribution of the acoustic field and the polarization direction of the shear wave, which can result in suboptimal detection performance. The acoustic field directivity of the shear wave generated by the butterfly coil electromagnetic acoustic transducer was measured using the transmission method. The data indicate that the acoustic pressure amplitude of the shear wave is maximized along the axis of the acoustic field, thereby meeting the requirements of synthetic aperture focusing technique imaging. We used the reflection method to detect the through-hole defects and investigated the effect of shear wave polarization direction. By comparing the experimental data and imaging results, it can be concluded that higher echo amplitudes are obtained when the polarization direction of the shear wave is perpendicular to the axis of the through-hole defects. Based on the explosive reflection model, the frequency domain phase shift migration (PSM) method converts the time-domain signal to the frequency domain for processing and uses a phase-shift factor for layer-by-layer imaging. We used the PSM method to process the experimental data, which not only produced high-resolution images but also had a high computational speed.

Published under an exclusive license by AIP Publishing. <https://doi.org/10.1063/5.0198404>

I. INTRODUCTION

The presence of defects significantly compromises the operational efficiency of components. Non-destructive testing technology can effectively identify these defects, thereby ensuring production safety. Common non-destructive testing techniques in the industry include ultrasonic testing (UT), radiographic testing (RT), magnetic particle testing (MT), penetration testing (PT), and microwave non-destructive testing (MNNDT).^{1,2} Among them, the ultrasonic testing technique offers extensive applicability, exceptional testing accuracy, cost-effectiveness, and safety throughout the testing process.³ Consequently, it has found extensive applications in the fields of aerospace engineering, medicine, building quality assessment, and industrial manufacturing.⁴

The electromagnetic ultrasonic testing technology is based on the principle of electromagnetic coupling to generate and receive ultrasonic waves without needing a coupling agent. It does not impose stringent requirements on the surface condition of the

workpiece, enabling non-contact measurements that are suitable for testing in high-temperature, high-speed, and other challenging environments.⁵ Depending on the testing requirements, various ultrasound waveforms can be generated in the workpiece by adjusting the coil type and manipulating the magnetic field direction in the electromagnetic acoustic transducer (EMAT).⁶ For instance, an improved longitudinal wave transducer with a circular coil is utilized between a magnetic rod and a ring-shaped magnet to measure the material's elastic constants.⁷ By employing a curved coil and arranging multiple face-to-face magnets, the amplitude of longitudinal waves can be enhanced by ~8.3 times.⁸ Guided waves can be excited using meander-line-coil surface wave EMATs combined with vertical magnetic field excitation surface waves, along with coiling the coil around a combination of inner and outer magnets.^{9,10} The more common shear wave EMAT uses a spiral coil, a race track coil, or a butterfly coil at the bottom and a permanent magnet structure at the top.¹¹

However, EMAT is affected by the structure, resulting in the transducer efficiency and sound field directivity being affected. Among them, Rueter investigated the effect of butterfly and spiral coils and found that the butterfly coil's main lobe currents are both unidirectional and parallel, and in mutual interference, they both produce the same magnetic effect (reverse eddy currents) in the target, whereas the magnetic effect produced by each coil of the spiral coil is weakened by the reverse current from the other side. Compared with spiral coils, butterfly coils can generate a larger coverage range and more concentrated energy, making them more advantageous in the detection process.¹² Zhang *et al.* introduced the structure of the butterfly coil, divided the butterfly coil into internal (main lobe area) and external (sidelobe area), and proved that it has high field density internally and low field density externally, the highest eddy currents and pressures are found at the main lobe position, and that the use of the butterfly coil can generate stronger eddy currents and higher Lorentz forces in the test samples.¹³ Zhou *et al.* measured the acoustic field directivity of the runway coil and found that the sound pressure value at the center axis of the EMAT radiated acoustic field was zero at any moment due to the opposite coil currents on the left and right sides of the runway coil.¹⁴

Since the butterfly coil sidelobes also exist in the current and are in the opposite direction to the main lobe current. Therefore, in the excitation process, if it is not shielded, the sidelobes also excite the ultrasonic waves, resulting in an unfocused sound field and poor directivity. The electromagnetic effect of the main lobe may also be weakened, reducing the efficiency of the transducer. Currently, the directivity of the acoustic field for EMATs that use only the main lobe of the coil as the working area is not clear. In addition, the shear wave has polarization characteristics; when the ultrasonic wave interacts with the material, its polarization state may affect the reflection, diffraction, transmission, and other phenomena caused by the impact. Therefore, defect detection needs to consider the sensitivity relationship between the polarization direction of the shear wave and the defects in order to improve the ability to identify specific types of defects and optimize the accuracy and imaging effect of defect detection.

Most conventional ultrasound imaging uses the B-scan imaging method, which summarizes the scan data and directly uses the sound pressure amplitude of the original signal for imaging, with poor imaging quality. However, defect detection based on electromagnetic ultrasonic transducers is limited by factors such as conversion efficiency and beam diffusion, resulting in a low signal-to-noise ratio of the defect signals.^{15,16} Moreover, during the inspection process of small-aperture EMAT of a single element, as the depth of the defect location increases, beam scattering occurs, resulting in a decrease in imaging resolution.¹⁷ The Synthetic Aperture Focusing Technique (SAFT) in ultrasonic inspection can compensate for the low resolution caused by this phenomenon. As a signal post-processing method, SAFT originally originated from synthetic aperture radar (SNR), applying the concept of "synthetic aperture" from SNR to the field of ultrasound imaging. The SAFT technique was later intensively studied and applied to medical ultrasonography and defect detection imaging. Compared to direct imaging, the SAFT effectively increases lateral resolution by treating a single-element transducer at different locations along the scan path as a large-aperture transducer.¹⁸ Initially, SAFT post-processing techniques primarily relied

on delay-and-sum (DAS) beamforming in the time domain. However, DAS typically necessitates a substantial number of computational operations during the imaging process, leading to prolonged computation times.

To reduce the significant computational time required for time domain DAS, the frequency domain SAFT was introduced to convert time domain data to the frequency domain.¹⁹ The phase shift migration (PSM) algorithm in the frequency domain is based on wave equation inversion theory, which directly performs a Fourier transform on ultrasound A-scan data. During the process, interpolation, filtering, and other processing are added before the inverse Fourier transform is performed. The processed information is then retransformed into the time domain to achieve image reconstruction. Skjelvareid *et al.* used a piezoelectric ultrasound probe to inspect pipes and performed imaging based on the frequency-domain PSM algorithm.²⁰ Ni *et al.* combined the PSM algorithm with laser ultrasound inspection to show the correct location of small defects in a three-dimensional manner and to improve the quality of the imaging.²¹ Due to the late development of electromagnetic ultrasound inspection technology, the previous reports on SAFT imaging technology have mainly focused on applications based on laser ultrasound and piezoelectric ultrasound, and there have been relatively few studies on the combination of electromagnetic ultrasound inspection technology and SAFT imaging technology.

In order to avoid the influence of the coil sidelobes on the radiated sound field, this paper proposes to shield the coil part except for the main lobe when designing the butterfly coil EMAT. Then an experimental system of acoustic field measurement was established to measure its acoustic field directivity. Subsequently, in order to verify the sensitivity of the shear wave polarization direction to the detection of defects in the through-hole, an experimental system of electromagnetic ultrasonic defect detection was built to verify the relationship between the defect detection sensitivity when the shear wave polarization direction is parallel and perpendicular to the direction of the through-hole axis, and the detection results were imaged and compared. Finally, in order to investigate the influence of defect location depth and defect size on the detection results, specimens containing defects of different depths and sizes were detected and imaged using B-scan, DAS, and PSM methods. After comparing the -6 dB width of defects, the superiority and feasibility of combining the frequency-domain PSM algorithm with butterfly coil EMAT were verified.

The paper is organized as follows: in Sec. II A, the 3D structural design of the improved butterfly coil and the 2D shielding model of the coil are presented, and the definition of the shear wave polarization direction for the two current modes of the butterfly coil and the working principle of EMAT are briefly described. The definition of imaging resolution is briefly described in Sec. II B. The principles of the DAS and PSM imaging algorithms in SAFT are described in detail in Sec. II C, and a comparison of the two algorithms is made, discussing the reasons for the high quality and speed of PSM compared to DAS imaging. The design of the acoustic field measurement experimental system and the electromagnetic ultrasonic defect detection system and their experimental programs are given in Sec. III. The directivity of the acoustic field in two polarization modes of EMAT is shown in Sec. IV A, and the effect of the shear wave polarization direction on the defect detection and imaging

results when it is parallel and perpendicular to the direction of the through-hole axis is discussed in Sec. IV B. The effect of defect depth on imaging effectiveness is discussed in Sec. IV C. In Sec. IV D, the imaging results of the different algorithms are compared, and the superiority of PSM over DAS in terms of resolution and position is verified by the normalized amplitude profiles after DAS and PSM processing. The imaging speed and defect localization accuracy of DAS and PSM are compared in Sec. IV E. Section V discusses the presented work and its conclusion.

II. THEORY

A. EMAT physical structure and detection principles

Since the sidelobes of the butterfly coil affect the energy distribution in the radiated sound field of the EMAT, in order to control the sound field of the butterfly coil EMAT and improve the acoustic directivity of the shear wave, this paper proposes to shield the rest of the butterfly coil except for the main lobe and only use the main lobe as the working area to stimulate the ultrasonic wave as an improvement scheme, and the shape of the magnets of the butterfly coil EMAT is optimized and designed. The 3D design of the transducer and its dimensions are shown in Fig. 1. The dimensions of the butterfly coil EMAT are $56 \times 56 \times 60 \text{ mm}^3$ ($L \times W \times H$), and a unipolar shaped permanent magnet is used inside. The shape of the permanent magnet is set as a convex shape in order to facilitate positioning and fixation, and the detailed design and dimensions of the permanent magnet are shown in Fig. 1(b). Below the magnet, the upper copper shielding layer, the butterfly coil, and the lower copper shielding layer are in order, and their three-dimensional structural design is shown in Fig. 1(c), in which the thickness of the coil and the copper shielding layer is 0.2 mm, and the upper copper shielding layer is used to reduce ultrasonic waves generated in the magnet, and the lower copper shielding layer is used to reduce the ultrasonic waves generated in the specimen by the butterfly coil sidelobes to avoid the influence on the acoustic field.

Based on the above design, the principle model of the improved butterfly coil EMAT for excitation of ultrasonic waves and the shielding schematic of the butterfly coil are shown in Fig. 2. Positioned beneath the permanent magnet, the main lobe of the butterfly

coil serves as a work area with dimensions of width (2a) and length (2b). The remaining sections of the coil are shielded with copper foil. The magnets are utilized to provide a static magnetic field or bias magnetic field, while the coil is stimulated with alternating pulse current to generate a dynamic magnetic field.²² When the current flows through the main lobe perpendicular to the plane of the paper, it generates a shear wave with a polarization direction parallel to the plane, as shown in Fig. 2(a). Conversely, when the current passes through the main lobe parallel to the plane of the paper, it generates a shear wave with a polarization direction perpendicular to that plane, as shown in Fig. 2(b).

The excitation of ultrasonic waves in non-ferromagnetic materials primarily relies on the Lorentz force, with the direction of ultrasonic wave propagation determined by both the orientation of the bias magnetic field and the current direction within the excitation coil.²³ By inputting high-frequency alternating current into the excitation coil, the alternating magnetic field B_d is induced around the coil. Under the effect of this alternating magnetic field, the aluminum plate generates an eddy current of the same frequency in the opposite direction. Moreover, an external bias magnetic field B_s is provided by a permanent magnet, which is oriented perpendicular to the surface of the object under investigation. Under the influence of a combined bias magnetic field and an alternating magnetic field, the specimen's surface experiences a Lorentz force perpendicular to the current direction. This induces particle vibrations within the specimen. Consequently, longitudinal waves and shear waves are excited, propagating along the thickness axis.²⁴ In the region where shear waves are excited on the surface layer of the workpiece, the magnetic induction intensity is B . The eddy current density induced in the main lobe part of the butterfly coil is J_e , which cooperates with the magnetic induction B to generate the Lorentz force, and the Lorentz force can be expressed as follows:²⁵

$$F_L = J_e \times B. \quad (1)$$

As the specimen is an elastic medium, the Lorentz force serves as the excitation force for ultrasonic waves. Consequently, internal particle vibrations within the specimen must conform to the wave

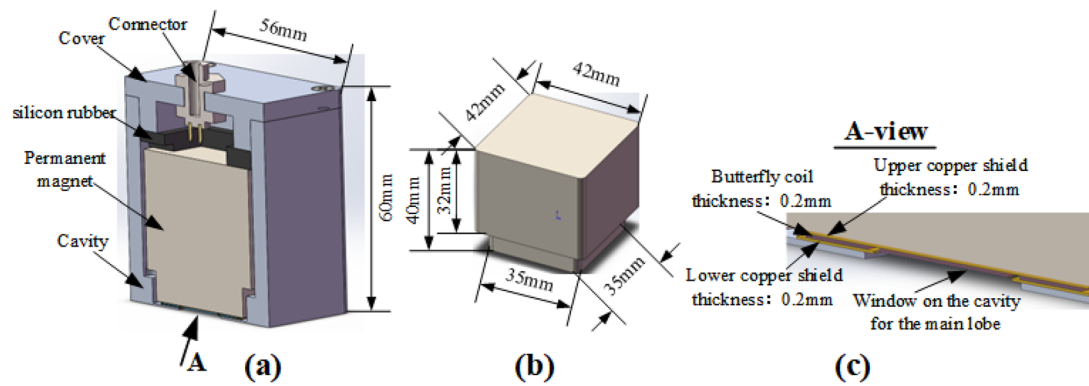


FIG. 1. Schematic design of butterfly coil EMAT structure. (a) Overall construction of EMAT. (b) EMAT's exterior design: The dimensions of the transducer are $56 \times 56 \times 60 \text{ mm}^3$ ($L \times W \times H$). (c) A view: the butterfly coil thickness is 0.2 mm and the copper shield thickness is 0.2 mm.

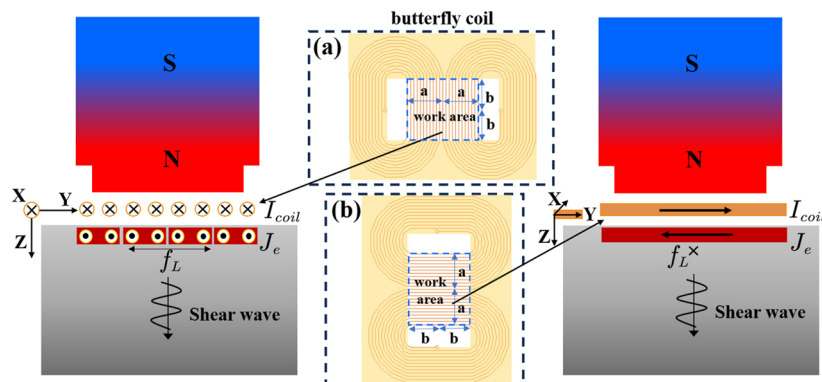


FIG. 2. Shear wave excitation process. (a) The direction of the current in the coil is perpendicular to the plane of the paper. (b) The direction of the current in the coil is parallel to the plane of the paper. The coil in both (a) and (b) is shielded, except for the rectangular work area.

equation in elastic dynamics, which is represented by the following equation:

$$\rho \frac{\partial^2 u}{\partial t^2} = (\lambda_m + 2\mu_m) \nabla(\nabla \cdot u) - \mu_m \nabla \times \nabla \times u + F_L, \quad (2)$$

where u represents the particle displacement vector, ρ denotes the specimen density, and λ_m and μ_m , respectively, stands for the Lamé constants. The presence of defects gives rise to an impedance mismatch along the wave propagation path, resulting in phenomena such as reflection, diffraction, interference, and scattering at the defect location.²⁶ By employing EMAT for receiving reflected shear waves and conducting signal analysis, valuable information regarding the defects can be obtained.

B. Lateral resolution

The lateral resolution is defined as the minimum distance between two targets that can be accurately distinguished in the lateral direction. A smaller value indicates a higher level of lateral resolution. The formula for lateral resolution is $\Delta x(z) = \frac{z \times \lambda}{A}$, where

Δx is directly proportional to the wavelength λ and the acoustic path z and inversely proportional to the aperture size A . The SAFT technique effectively enhances lateral resolution by equating individual small aperture transducers positioned at various locations along the scanning path with a large aperture transducer, thereby increasing the aperture size.²⁷

C. Imaging methods

The B-scan imaging is presented as a two-dimensional image, which is obtained by collating multiple A-scan ultrasound data acquired along the EMAT scan path. The SAFT technique leverages information obtained from reflections in multiple directions to enhance the internal defect information within the specimen. By superimposing this information, the amplitude of defect signals becomes significantly higher than that of defect-free areas, thereby enhancing the image quality.²¹ The DAS principle is illustrated in Fig. 3(a). Ultrasonic excitation is shown by the orange arrow labeled with the letter "E," and detection is shown by the green arrow labeled with the letter "D."²⁸ The principle of the DAS algorithm begins by discretizing the region of the specimen to be measured into $x * z$ cells

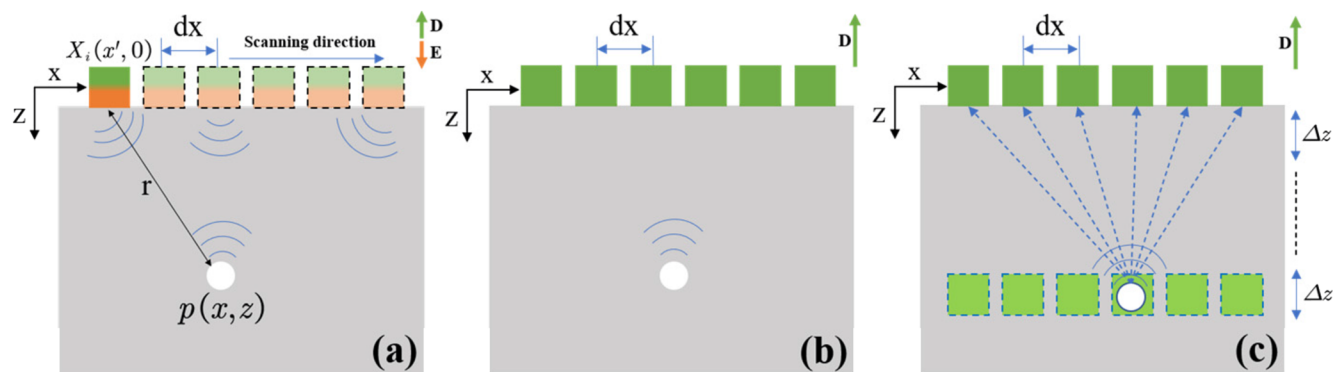


FIG. 3. Illustration of SAFT. (a) The B-scan process involves a single-element transducer that moves along the X-axis, sequentially exciting and receiving ultrasonic waves; (b) the backpropagation model; and (c) the phase shift migration model.

in the Cartesian coordinate system.²⁹ Assuming the point $Q(x, z)$ in the diagram serves as the focal point for imaging, $X_i(x', 0)$ represents the coordinates of the transducer's detection position. We consider the propagation of ultrasonic waves in a medium as a direct wave, and the ultrasonic wave speed is denoted by c' . Since the received shear wave is a reflection echo, the acoustic range of the ultrasonic wave is twice the distance from the detection point to the target point. Therefore, we take the equivalent wave velocity c as half of the actual measured wave velocity c' .³⁰ The propagation time from the detection point $X_i(x', 0)$ to the target point $Q(x, z)$ is given by the following equation:

$$t_{x,z} = \frac{\sqrt{(x-x')^2 + z^2}}{c}. \quad (3)$$

The amplitude of every discrete cell can be obtained by superimposing the echo signal amplitudes of the A-scan data with the corresponding delay.³¹ The formula for the superposition is given by the following equation:

$$I(x, z) = \sum_{i=1}^N M_i(t_{x,z}), \quad (4)$$

where $M_i(t_{x,z})$ denotes the reflected echo signal strength from point (x, z) received by the transducer at each detection position, i denotes the positional order of the transducer in the detection path, and N denotes the total number of positions received by the transducer. For the same set of A-scan data, the computational workload for DAS imaging exhibits a linear multiplicative increase in proportion to the number of pixel points.

The PSM algorithm is based on the principle of backpropagation, as illustrated in Fig. 3(b). When the ultrasonic wave reflects at the defect location, we consider this reflection point as a new source emitting ultrasonic waves onto the testing surface.³² At the critical state of the explosion reaction, when $t = 0$, the transducers would receive an ultrasound signal with maximum amplitude. The frequency domain PSM algorithm discretizes the data in time and space, employing $p(t, x, z)$ to represent the temporal variation of sound pressure amplitude at any given point $Q(x, z)$ within the imaging area.³³ In geometry, the solution of the scalar wave equation is represented as a plane wave,

$$p(t, x, z) = k \times e^{i(k_x x + k_z z - \omega t)}, \quad (5)$$

where k is the positive correlation coefficient; k_x and k_z represent the wave number components in the X and Z directions; and k_x , k_z , and ω satisfy the dispersion relation,

$$\frac{\omega^2}{c^2} = k_x^2 + k_z^2. \quad (6)$$

Only two of the three variables are independent of each other, with k_z as the only dependent variable. The combination of all general solutions to the wave equation is shown in the following equation:

$$p(t, x, z) = \int \int_{-\infty}^{\infty} A(\omega, k_x) \times e^{i(k_x x + k_z z - \omega t)} dk_x d\omega, \quad (7)$$

where $A(\omega, k_x)$ denotes the complex amplitude of each (ω, k_x) combination. The combination of the $A(\omega, k_x)$ and $e^{ik_z z}$ terms is denoted as $P(\omega, k_x, z)$. As shown in Eq. (8), the Fourier inverse transform can be used to solve for $P(\omega, k_x, z)$,³⁴

$$p(t, x, z) = \int \int_{-\infty}^{\infty} P(\omega, k_x, z) \times e^{ik_x x} \times e^{-i\omega t} dk_x d\omega. \quad (8)$$

$P(\omega, k_x, z)$ in Eq. (8) denotes the acoustic field of $p(t, x, z)$ in the frequency domain. Figure 3(c) illustrates the process of wavefield extrapolation, which involves simulating a virtual array of sensors within the specimen. As described in Eq. (9), multiplying the frequency-domain acoustic field $P(\omega, k_x, z)$ obtained at $Z = 0$ with the phase-shift factor $e^{ik_z \Delta z}$ gives the frequency-domain acoustic field at z depth, where Δz can be expressed as $z - Z$,

$$P(\omega, k_x, z) = P(\omega, k_x, Z) \times e^{ik_z \Delta z}. \quad (9)$$

Under the imaging condition $t = 0$, the focused image line of this deep layer can be calculated from the following equation:

$$I(x, z) = \int \int_{-\infty}^{\infty} P(\omega, k_x, Z) \times e^{ik_z(z-Z)} \times e^{ik_x x} dk_x d\omega, \quad (10)$$

the focused image of the entire area can be obtained by performing phase-shift calculations for every depth of interest.²⁰

From the discussion of these two imaging methods, it can be concluded that the DAS algorithm takes the signal received by the transducer at a single detection position as the full sound field and calculates the sound pressure amplitude at the delay time. However, due to the transducer's small size, the sound field it receives is not representative of the actual full sound field, leading to inaccuracies and unnecessary noise. Furthermore, if there is significant noise in the signal, the superimposed noise can cause unnecessary artifacts in the image. On the other hand, based on the principle of explosion reflection, PSM technology uses the phase information in ultrasonic wave propagation to extrapolate the wave field, and the resulting sound field is equivalent to the scatterer radiation sound field recorded by the virtual probe array at different depths. By employing the principle of explosive reflection, it simulates the transducer receiving the wave field emitted by reflectors within the specimen. This enhances the signal strength of the wave field at each focal depth, thereby improving the signal intensity at the defect location. This technique effectively sharpens the boundary of the defect and enhances resolution.

In contrast, the PSM algorithm can make better use of phase information and improve the accuracy of beam formation, whereas, in the original signal processing stage, the DAS algorithm only uses a bandpass filter for filtering. In the PSM algorithm, by analyzing the signal in the frequency domain before the phase shift, the use of matched filters on the original signal preprocesses noise reduction, which can effectively improve the impact of the noise on the imaging. Therefore, the frequency domain PSM algorithm is superior in imaging resolution and positional accuracy compared to the time domain DAS algorithm. In addition, since the DAS algorithm needs to utilize the data obtained from all detection positions to superimpose the target points in the entire imaging region after delay calculation one by one, the calculation often requires multiple iterations, and the computational time-consumption grows

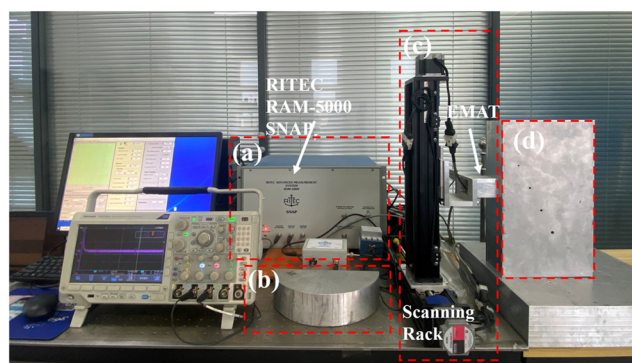


FIG. 4. Diagram of the experimental platform. (a) RITEC RAM-5000 SNAP nonlinear high-energy ultrasonic testing system, (b) semicircular aluminum specimen for acoustic field directivity experiments, (c) 2-D scanning rack for mobile EMAT, and (d) rectangular aluminum specimen for defect detection experiments.

tremendously with the increase in the data volume, whereas the PSM algorithm is processed in the frequency domain, utilizing the phase relationship of the signals and reconstructing layer by layer by means of the phase-shift factor, and the computational speed of PSM is significantly faster than DAS.

Therefore, this paper proposes to use the PSM method to image the experimental results and compare them with B-scan imaging and DAS imaging to verify the advantages of the PSM imaging algorithm.

III. EXPERIMENTAL

A. Experimental system

The physical diagram of the EMAT system is depicted in Fig. 4, which contains the RITEC RAM-5000 study of nonlinear acoustic phenomena (SNAP) nonlinear high-energy testing ultrasonic system used to realize the experiments in this study. In addition, the experimental setup includes a 2D scanning device, a butterfly coil EMAT, a semicircular specimen, and three rectangular specimens with through-hole defects. The butterfly coil possessed a working area width ($2a$) of 11 mm and length ($2b$) of 10 mm. The semicircular and rectangular specimens were fabricated from Al 6061-T6.

The experiments conducted are as follows: Experiment 1 measures the directivity of the shear wave acoustic field using the transmission method, while experiment 2 detects defective specimens using the reflection method. The experimental system for shear wave acoustic field directivity is shown in Fig. 5. The experimental equipment comprises a computer, RITEC RAM-5000 SNAP nonlinear high-energy ultrasonic testing system, butterfly coil EMAT, and oscilloscope, as well as a semicircular aluminum specimen with a thickness of 60 mm and a radius of 120 mm. The defect detection experimental system is depicted in Fig. 6. It incorporates a two-dimensional scanning device added to the previously mentioned experimental equipment. All three specimens were aluminum plates with dimensions of $350 \times 200 \times 35$ mm 3 , each containing four through-hole defects. Visual representations of the specimens can be seen in Figs. 6(b)–6(d), and their design scheme is shown in Fig. 7.

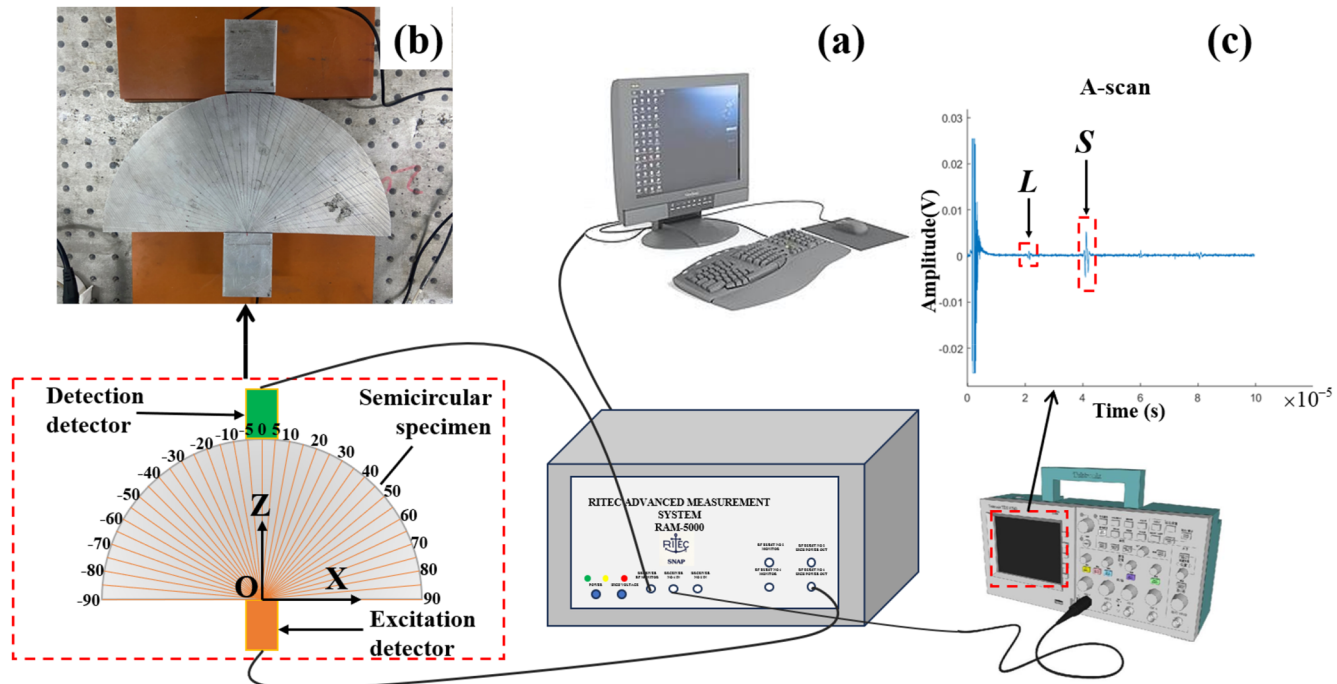


FIG. 5. Diagram of the experimental model of acoustic field directionality. (a) The experimental equipment, (b) the semicircular aluminum specimen, as well as the excitation and reception EMATs employed in the experiment, and (c) the A-scan data acquired by an oscilloscope.

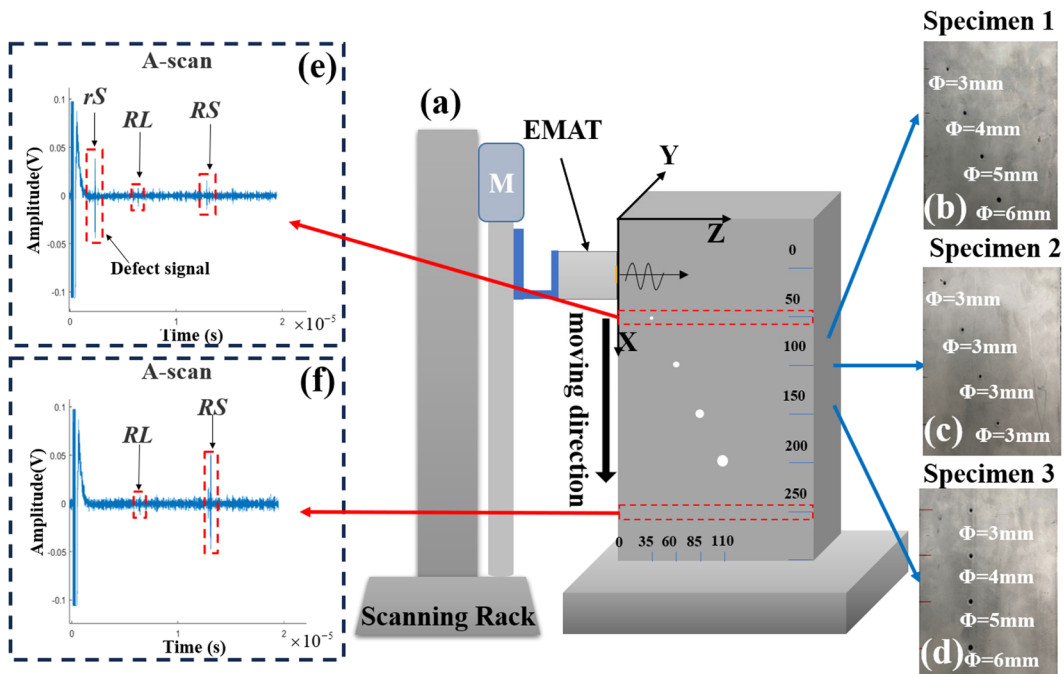


FIG. 6. Diagram of the defect detection experiment platform. (a) Experimental equipment, (b)–(d) experimental specimen with different through-hole defects, (e) A-scan waveforms detected by EMAT above the defects, and (f) A-scan waveforms detected by EMAT in the absence of defects.

B. Experimental program

The acoustic field directional measurement is conducted by positioning the excitation EMAT at the center of a semicircular aluminum specimen and situating the receiving EMAT around its circumference. The detection range spans from -90° to 90° , with direct ultrasonic waves being received at 5° intervals. The directivity of shear waves in two polarization directions is measured by rotating the probe in the semicircular plane of the aluminum specimen

at a working frequency of 2 MHz.³⁵ The sampling interval of the oscilloscope was 20 ns. To minimize the interference of noise on the effective signal and obtain more stable experimental data, the data were saved after averaging 64 times on the oscilloscope. Figure 5(c) illustrates the direct waves received by the receiving and excitation transducers positioned along the same axis. In this figure, *L* and *S* represent longitudinal and shear waves, respectively. It is worth noting that the amplitude of the longitudinal wave signal exhibits

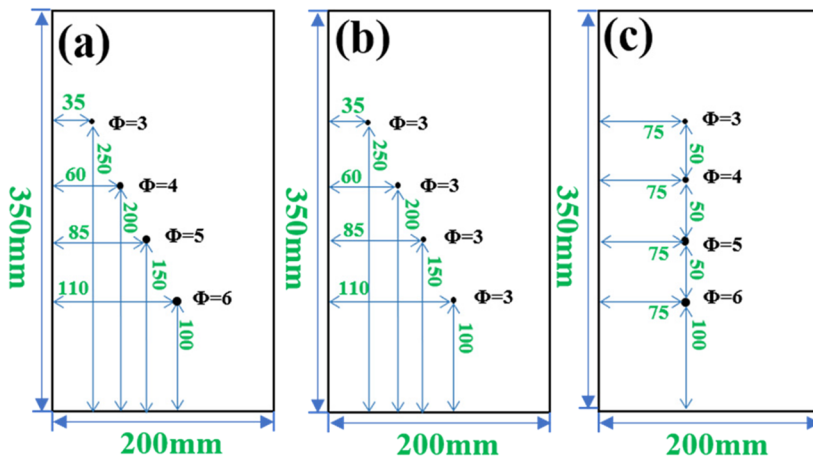


FIG. 7. Specimen design. (a) Specimen 1, (b) specimen 2, and (c) specimen 3.

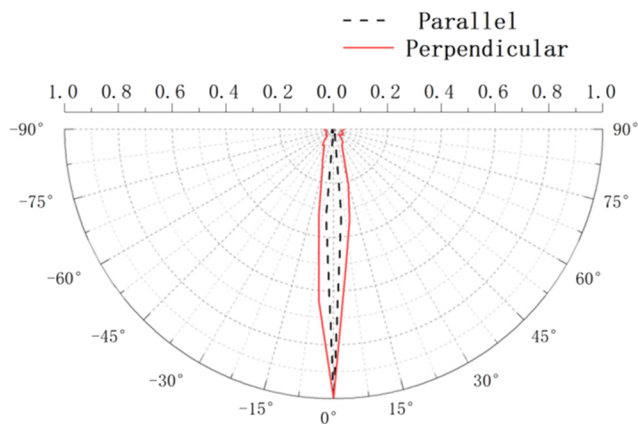


FIG. 8. Shear wave directivity patterns. The black delineation and the red curve indicate the directivity diagram of the shear wave when the polarization direction is parallel and perpendicular to the semicircular plane of the aluminum specimen, respectively.

a significant reduction compared to that of the shear wave. In the experiment for defect detection, the EMAT is attached to the mobile platform of the 2-D scanning device to precisely control the EMAT in the B-scan along the X-axis direction of the specimen. The scanning length is 250 mm, with a step size of 0.5 mm, resulting in a collection of 501 echo signals. Measurements were conducted in two distinct polarization directions of shear waves for each specimen. Figures 6(e) and 6(f) display the A-scan waveforms detected by the EMAT above the defect and in the absence of a defect, respectively. The labels *rS*, *RL*, and *RS* in these figures represent the reflected shear wave from the defect, the bottom-reflected longitudinal wave, and the bottom-reflected shear wave, respectively.

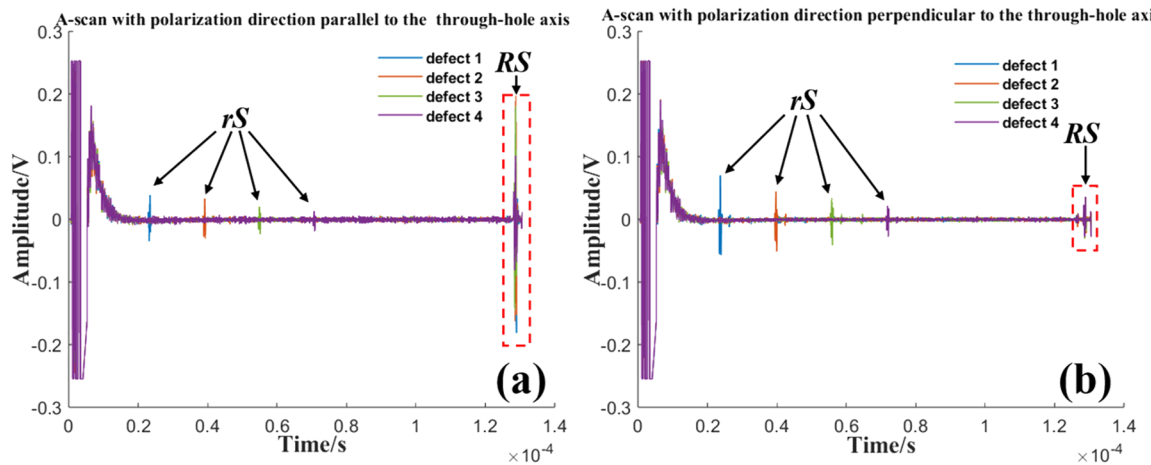


FIG. 9. A-scan waveforms were obtained at different polarization directions. (a) A-scan signals are detected above each defect when the polarization direction of the shear wave is parallel to the axis direction of the through-hole. (b) A-scan signals are detected above each defect when the polarization direction is perpendicular to the axis direction of the through-hole.

TABLE I. Peak-to-peak value of the measured sound pressure amplitude when the polarization direction of the shear wave is parallel or perpendicular to the axis direction of the through-hole.

	Defect 1 (V)	Defect 2 (V)	Defect 3 (V)	Defect 4 (V)
Parallel	0.073	0.063	0.044	0.031
perpendicular	0.126	0.095	0.075	0.048

IV. ANALYSIS OF RESULTS

A. Directivity of the acoustic field

By analyzing the propagation time of the shear wave in the A-scan waveform, we calculated a propagation speed of ~ 3130 m/s. The signals received underwent preprocessing by applying a band-pass filter to enhance the signal-to-noise ratio of the A-scan. Then, the signal was intercepted based on the propagation time of the shear wave, and its peak-to-peak value was computed. These values were normalized and plotted in a polar coordinate system to plot the directivity pattern specific to the shear wave produced by the butterfly coil EMAT, as shown in Fig. 8. The acoustic field of the shear wave is symmetrical, with the majority of its energy concentrated within the angular range of $(-10^\circ, 10^\circ)$ and reaching maximum intensity in the 0° direction. It is important to note that all evaluations presented are objective and supported by evidence. When the testing probe passes over a defect, the amplitude of the shear wave signal undergoes significant changes, meeting the prerequisites for synthetic aperture-focused imaging.

B. The influence of shear wave polarization direction on imaging

Adjusting the orientation of the butterfly coil enables various polarization directions for the shear wave. When the current flows parallel to the X-axis, the shear wave polarization direction is aligned

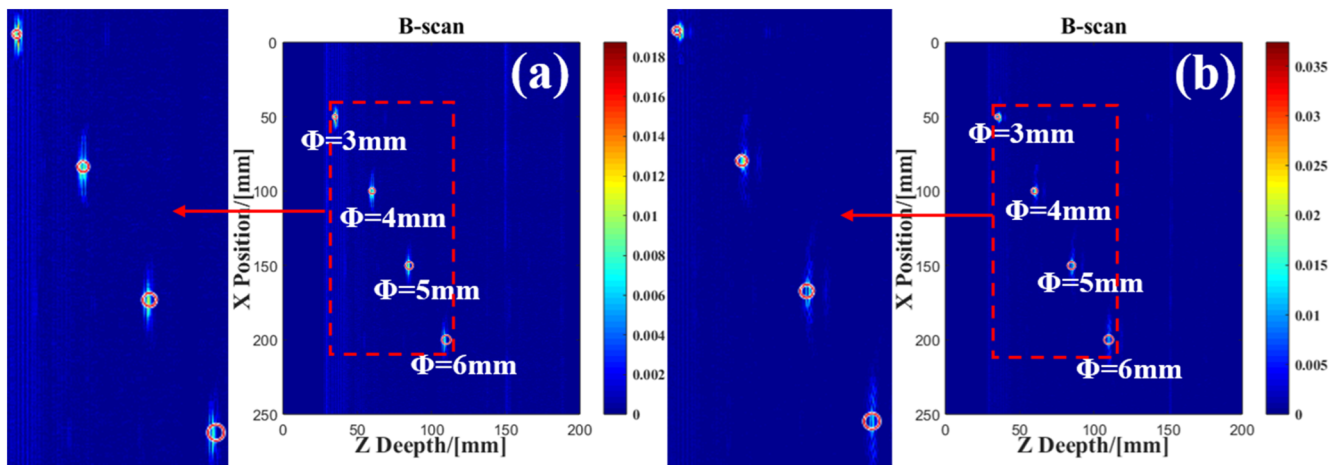


FIG. 10. B-scan images of specimen 1. (a) B-scan image obtained by the polarization direction of the shear wave parallel to the direction of the through-hole axis. (b) B-scan image obtained by the polarization direction perpendicular to the direction of the through-hole axis. The red circles in all subsequent images represent the real size and position of the defect.

with the through-hole axis, whereas when it flows parallel to the Y-axis, it becomes perpendicular to that axis. The A-scan data for specimen 1 were examined in both polarization directions and are presented in Fig. 9. Table I shows the peak-to-peak values of the echoes corresponding to each defect. Notably, the values of the echo signals exhibit a significantly higher magnitude when the polarization direction of the shear wave is perpendicular to the through-hole axis compared to when it is parallel. The B-scan, DAS algorithm, and PSM algorithm were used to image the test data of specimen 1, as shown in Figs. 10–12, under different shear wave polarization directions. It can be observed that buried defects within the specimen can be detected in both shear-wave polarization orientations. However, there is a notable divergence in their size and shape within the im-

aging results. In Figs. 10(a)–12(a), a hyperbolic pattern is present in the shape of the defect. The ability to focus is poor, making it difficult to determine the precise location and shape of the defect from the image alone.³⁶ In contrast, Figs. 10(b)–12(b) display narrower lateral widths and clearer edges.

Based on the A-scan waveforms and imaging results of shear waves in two different polarization directions, it is clear that when the polarization direction is perpendicular to the through-hole axis, the defect boundaries reflect most of the shear wave energy. This results in stronger echo amplitudes. In this scenario, imaging defects parallel to the through-hole axis after DAS and PSM processing result in higher lateral resolution and more concentrated detection capabilities. In contrast, when the polarization direction of shear

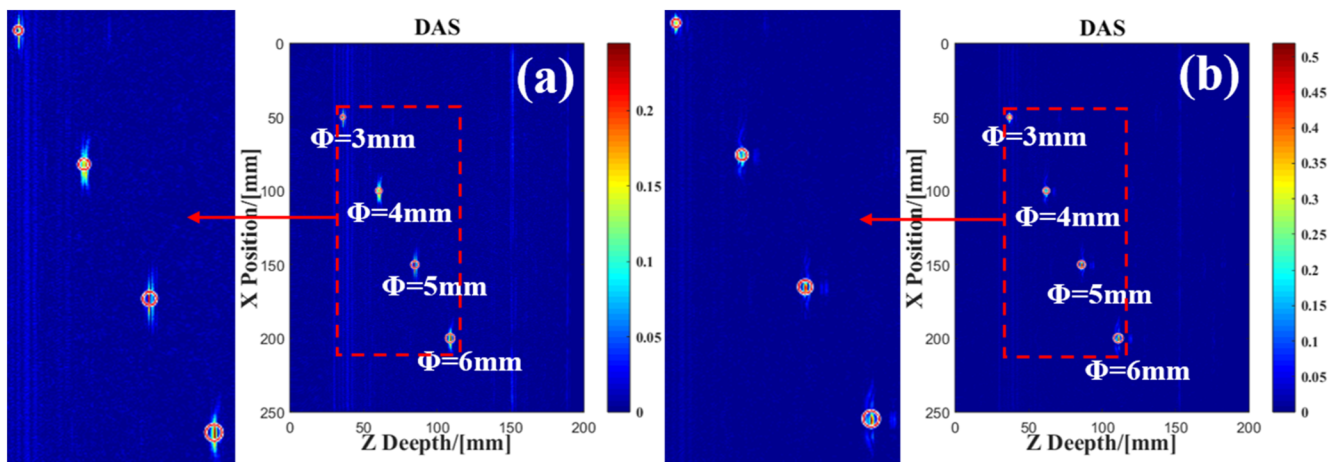


FIG. 11. DAS images of specimen 1. (a) DAS image obtained when the polarization direction of the shear wave is parallel to the direction of the through-hole axis. (b) DAS image obtained when the polarization direction is perpendicular to the direction of the through-hole axis.

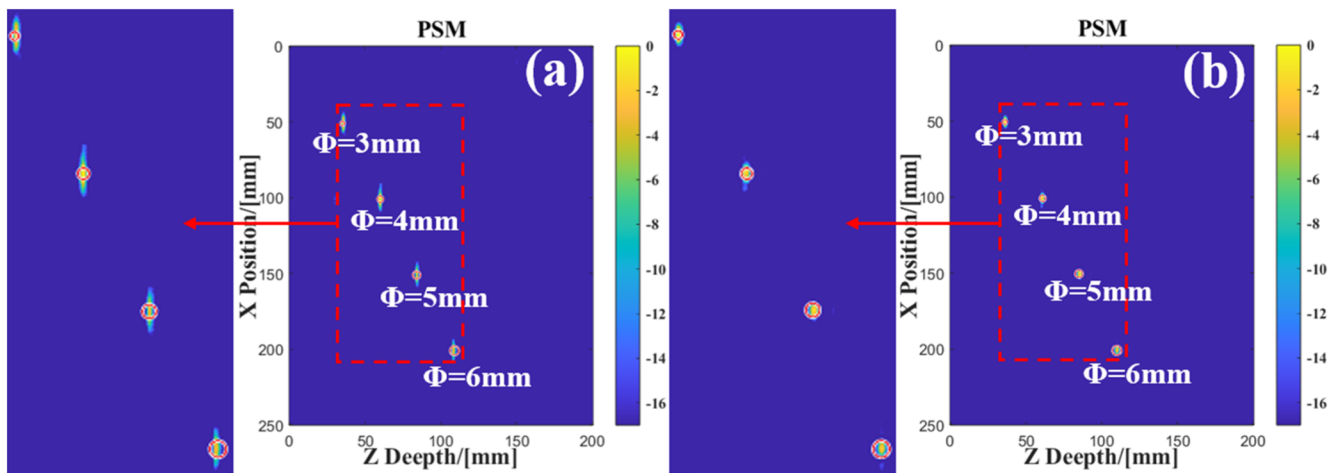


FIG. 12. PSM images of specimen 1. (a) PSM image obtained when the polarization direction of the shear wave is parallel to the direction of the through-hole axis. (b) PSM image obtained when the polarization direction is perpendicular to the direction of the through-hole axis.

waves is parallel to the axis of the through-hole, a significant amount of shear wave can easily pass through the defect and reach the bottom, resulting in a strong bottom-reflected shear wave. However, the signals reflected from the defect are relatively weak.³⁷ Despite the implementation of DAS and PSM processing, satisfactory results are not achieved, which hampers defect detection imaging.

C. The influence of defect depths on imaging

To examine the depth-dependent effect of single-element EMAT detection and confirm the enhanced imaging quality attributed to SAFT, experiments were performed on specimen 2. The polarization direction of the shear wave is perpendicular to the axis of the defect through-hole. The experimental data were processed and imaged, and the imaging results are presented in

Fig. 13. Furthermore, it presents an enlarged view of defect 4 within each imaging algorithm. By comparing the imaging results for each defect, a distinct pattern becomes apparent. With increasing depth of the defect, the B-scan imaging exhibits a gradual attenuation in signal amplitude and an augmented lateral width dispersion. Defect 4 in Fig. 13(a) is an elongated band that diverges toward both ends. The DAS imaging results exhibit a higher concentration of energy in the defects. Defects 1 and 3 are nearly identical in size. The sizes of each defect in the PSM imaging results closely correspond to their actual sizes, with defect 4 exhibiting a contour that aligns precisely with the red circle.

To quantitatively measure the effectiveness of the imaging, we will use the full width at half maximum (FWHM) of each echo peak, also known as the -6 dB width, as a quantitative measure of the

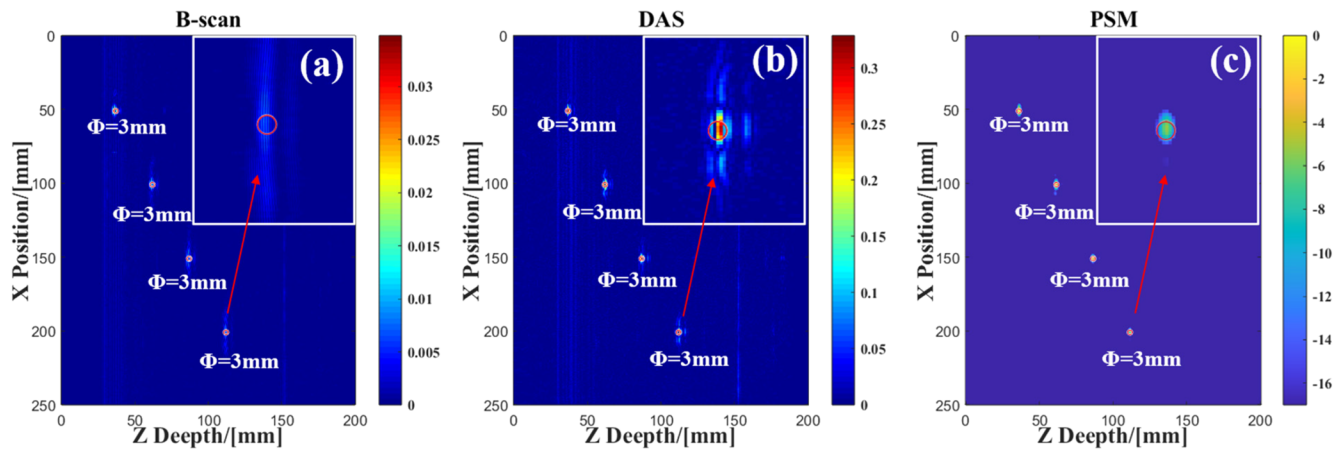
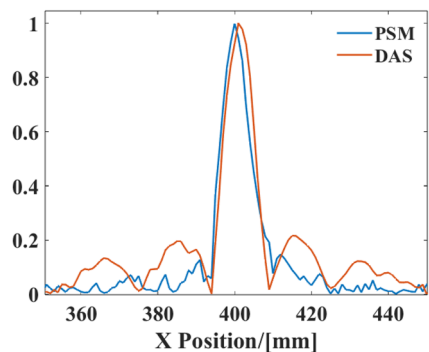


FIG. 13. Specimen 2 imaging results. (a)–(c) Are the B-scan, DAS, and PSM images detected when the polarization direction of the shear wave is perpendicular to the axis direction of the through-hole.

TABLE II. -6 dB width of each defect in specimen 2.

Imaging methods	Defects	Depth (mm)	Actual size (mm)	-6 dB width (mm)
B-scan	1	35	3	4.3
	2	60	3	5.2
	3	85	3	7.1
	4	110	3	8.2
DAS	1	35	3	5.8
	2	60	3	5.6
	3	85	3	5.7
	4	110	3	5.5
PSM	1	35	3	4.4
	2	60	3	4.2
	3	85	3	4.5
	4	110	3	4.3

**FIG. 14.** Comparison of normalized amplitude profile plots from the DAS images and the PSM image.

defects.³⁸ Table II shows that the -6 dB width of the B-scan increases with depth. Upon processing with the DAS algorithm, defects 3 and 4 show a reduction in their respective -6 dB widths by $\sim 20\%$ and 33% compared to the B-scan imaging results. The PSM algorithm further reduces the size by $\sim 24\%$ and 48% compared to the B-scan imaging results. These results indicate that as depth increases, the EMAT of a single element is influenced by acoustic beam diffusion, which increases the lateral width of defects. However, the effective application of SAFT processing mitigates this effect and leads to a significant improvement in lateral resolution.

By integrating the preceding analyses, it becomes evident that there are obvious artifacts on both sides of the defect in the DAS image. Conversely, no comparable artifacts are discernible in the PSM outcomes. To delve deeper into the comparison between DAS and PSM, we plotted normalized amplitude profiles for both image types. Figure 14 illustrates the results, clearly revealing that DAS imaging generates high-amplitude sidelobes, whereas PSM results exhibit a low-amplitude sidelobe.³⁰ Notably, after PSM processing, the -6 dB width of defect 4 measures just 4.3 mm, whereas it measures 5.5 mm after DAS processing. These findings underscore subtle yet significant differences in image quality between DAS and PSM, highlighting PSM's capability to effectively minimize sidelobes and enhance image resolution. Furthermore, PSM not only reduces sidelobes but also achieves a -6 dB width closer to the actual defect size, thereby offering superior imaging clarity.

D. Imaging of different defect sizes

We analyzed specimen 3 to evaluate the imaging performance of different imaging methods for defects with varying apertures and presented the corresponding imaging results in Fig. 15. Which clearly shows that the lateral width of the defects increases proportionally with their respective diameters. All three imaging results exhibit a similar pattern, with SAFT treatment yielding superior imaging compared to the B-scan, consistent with our previous discussion. The defect contour in Fig. 15(c) notably exhibits a close alignment with the red circle marker.

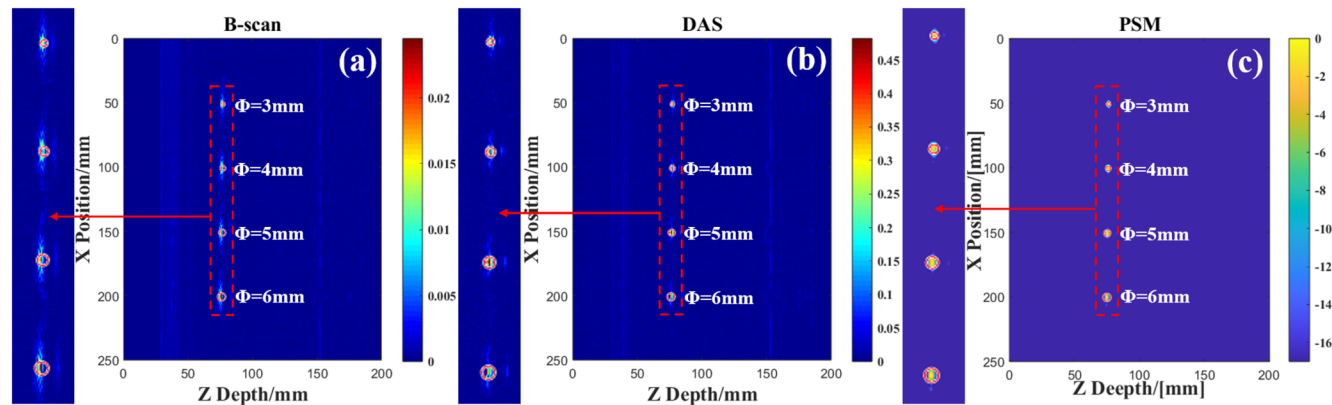
**FIG. 15.** Specimen 3 imaging results. (a)–(c) Are the B-scan, DAS, and PSM images detected when the polarization direction of the shear wave is perpendicular to the axis direction of the through-hole.

TABLE III. –6 dB width of each defect in specimen 3.

Imaging methods	Defects	Depth (mm)	Actual size (mm)	–6 dB width (mm)
B-scan	1	75	3	4.3
	2	75	4	5.8
	3	75	5	7.1
	4	75	6	8.8
DAS	1	75	3	4.1
	2	75	4	4.7
	3	75	5	5.3
	4	75	6	5.2
PSM	1	75	3	3.5
	2	75	4	4.2
	3	75	5	5.1
	4	75	6	5.9

The –6 dB width for each defect in specimen 3 is provided in **Table III**. The table data indicate a positive correlation between the actual sizes and the imaging sizes. However, there is some measurement error between the –6 dB width of the defect and the actual size. In particular, the error rate for B-scan imaging results is over 40%, whereas DAS imaging results have an error rate below 30%. Conversely, PSM imaging demonstrates a significantly lower error rate of only 10%.

E. Imaging accuracy and speed

To confirm the accuracy of defect localization, we performed a comparative analysis of the three imaging results obtained from specimen 1. We extracted the pixel amplitudes surrounding the defect points in each result and identified the highest value point in this area as the central position of the defect. The measured coordinates of the defect locations are presented in **Table IV**. The B-scan's error range in the depth direction is observed to be between 0.2 and 1.3 mm, while the lateral error remains within 1 mm. After processing with the DAS algorithm, the depth direction error is reduced to within 1 mm, and the lateral error is constrained to 0.5 mm. Employing the PSM algorithm effectively constrains the depth and lateral errors within a narrow range of 0.5 mm, thereby significantly augmenting the accuracy of imaging features.

To ensure a precise comparison of the imaging speeds between the two SAFT algorithms, we utilized an identical computer system and operating environment to process the data from specimen 1. In

addition, the resolution of the image and the amount of data being processed have an impact on both the quality of the image and the time required for processing. When the scanning step is 1 mm, the DAS algorithm produces images with a minimum pixel size of mm², and the reconstruction process takes ~210 s. In contrast, the PSM algorithm completes the same task in only 0.12 s. When the scanning step is 0.5 mm, the DAS algorithm takes ~1900 s to process, while the PSM algorithm completes the task in just 0.3 s.

V. CONCLUSION

This research is based on the butterfly coil EMAT, which employs copper foil to shield all components except for the main lobe, thus ensuring that it serves as the working area. The directivity of the shear wave field was assessed across two distinct polarization directions, revealing maximum acoustic pressure values aligned along the acoustic field's axis. Rectangular aluminum specimens with through-hole defects were measured by shear wave reflection, and the experimental data were processed for B-scan and SAFT imaging. According to the analysis of the data and images, a decrease in the echo amplitude of the defect is observed when the polarization direction of the shear wave aligns parallel to the axis of the through-hole. However, it is noteworthy that there is no significant improvement in lateral resolution after SAFT processing. Consequently, this approach does not facilitate effective defect detection. When the polarization direction of the shear wave is perpendicular to the axis of the through-hole, both DAS imaging and PSM imaging effectively enhance lateral resolution. After applying the PSM, the –6 dB width decreased by ~40% compared to B-scan imaging. The PSM imaging results exhibit alignment with actual conditions owing to the enhanced clarity of defect contours and improved accuracy in positioning. Under the same conditions, PSM demonstrates significantly higher computational efficiency, over 6000 times faster than the DAS algorithm.

ACKNOWLEDGMENTS

The work was supported in part by the Natural Science Foundation of Shandong Province, China (Project No. ZR2023ME073); the National Natural Science Foundation of China (Project No. 51805304); the Education Department of Shandong Province, China (Project No. 2022KJ130); Qilu University of Technology (Shandong Academy of Sciences), China (Project Nos. 2023PY009, 2021JC02008, and 2022GH005); and the Science and Technology Small and Medium Enterprises Innovation Capacity Improvement Project of Shandong Province, China (Project No. 2023TSGC0731).

AUTHOR DECLARATIONS

Conflict of Interest

The authors have no conflicts to disclose.

Author Contributions

Chaoqun Wang: Writing – original draft (lead). **Jian Ma:** Conceptualization (lead); Methodology (lead); Writing – review & editing

TABLE IV. Actual and imaged positions of defects in specimen 1.

Defects	Actual position	B-scan	DAS	PSM
1	(35, 50)	(36.3, 51)	(36, 50.5)	(35.5, 50)
2	(60, 100)	(60.9, 101)	(61, 100.5)	(60.5, 100.5)
3	(85, 150)	(85.6, 150.5)	(86, 150)	(85.5, 150)
4	(110, 200)	(110.2, 200.5)	(111, 200.5)	(110, 200)

(lead). **Xue Bai**: Data curation (lead); Writing – review & editing (equal). **Jianwei Chen**: Data curation (equal); Methodology (equal).

DATA AVAILABILITY

The data that support the findings of this study are available from the corresponding author upon reasonable request.

REFERENCES

- ¹A. Hosoi, Y. Yamaguchi, Y. Ju, Y. Sato, and T. Kitayama, *Compos. Struct.* **128**, 134 (2015).
- ²Z. Y. Lu, Q. L. Zhang, and X. Liu, Proceedings of International Conference on Intelligent Systems Design and Engineering Applications (IEEE Computer Society 2013), 403 (n.d.).
- ³H. R. Jin, Z. S. Zheng, X. Q. Liao, and Y. J. Zheng, *Mech. Syst. Signal Process.* **168**, 108654 (2022).
- ⁴O. S. Amosov, S. G. Amosova, and I. O. Iochkov, *IFAC-PapersOnLine* **54**, 484 (2021).
- ⁵M. Seher and P. B. Nagy, *NDT&E Int.* **84**, 1 (2016).
- ⁶J. Parra-Raad, Ph.D. thesis, Department of Mechanical Engineering, Imperial College London, London, 2011.
- ⁷M. P. Da Cunha and J. W. Jordan, in *Proceedings of IEEE International Frequency Control Symposium and Exposition* (IEEE, 2005), p. 426.
- ⁸G. Dang, C. Pei, T. Liu, C. Xie, D. Liu, and Z. Chen, *IEEE Sens. J.* **22**(20), 19424 (2022).
- ⁹L. Kang, S. Dixon, K. Wang, and J. Dai, *NDT&E Int.* **59**, 11 (2013).
- ¹⁰H. M. Seung, C. I. Park, and Y. Y. Kim, *Ultrasonics* **69**, 58 (2016).
- ¹¹R. B. Thompson, in *Ultrasonic Measurement Methods*, edited by R. N. Thurston and A. D. Piercer (Academic Press, New York, 1990), Vol. 19, Part 4.
- ¹²D. Rueter, *Ultrasonics* **65**, 200 (2016).
- ¹³J. J. Zhang, M. Liu, X. J. Jia, and R. Z. Gao, *Sensors* **22**(13), 4985 (2022).
- ¹⁴J. J. Zhou, H. D. Jia, Y. Zheng, and Z. J. Zhang, *J. Mech. Eng.* **56**(2), 9–19 (2020).
- ¹⁵H. Y. Sun, S. Wang, S. L. Huang, L. S. Peng, Q. Wang, W. Zhao, and J. Zou, *IEEE Sens. J.* **20**(12), 6295 (2020).
- ¹⁶W. Z. Shi, Y. S. Tong, C. Lu, Y. Chen, G. Shen, and G. D. Zeng, *Ultrasonics* **124**, 106729 (2022).
- ¹⁷Y. Tasinkevych, I. Trots, A. Nowicki, and P. A. Lewin, *Ultrasonics* **52**(2), 333 (2012).
- ¹⁸T. Stepinski, *IEEE Trans. Ultrason., Ferroelectr., Freq. Control* **54**, 1399 (2007).
- ¹⁹T. Stepinski and F. Lingvall, in *Proceedings of IEEE Ultrasonics Symposium* (IEEE, 2004), p. 701.
- ²⁰M. H. Skjelvareid, Y. Birkeland, and Y. Larsen, *IEEE Trans. Ultrason., Ferroelectr., Freq. Control* **59**(11), 2460 (2012).
- ²¹C. Y. Ni, C. Chen, K. N. Ying, L. N. Dai, L. Yuan, W. W. Kan, and Z. H. Shen, *Photoacoustics* **22**, 100248 (2021).
- ²²S. L. Huang, Z. Wang, S. Wang, Q. Wang, and W. Zhao, *Rev. Sci. Instrum.* **92**(2), 025006 (2021).
- ²³R. Ribichini, F. Cegla, P. B. Nagy, and P. Cawley, *NDT&E Int.* **45**, 32 (2012).
- ²⁴H. Ogi, *J. Appl. Phys.* **82**, 3940 (1997).
- ²⁵L. Xiang and R. S. Edwards, *J. Nondestr. Eval.* **39**, 9 (2020).
- ²⁶Z. Q. Xue, Y. D. Xu, M. Hu, and S. Z. Li, *Constr. Build. Mater.* **368**, 130409 (2023).
- ²⁷M. Karaman, P. C. Li, and M. O'Donnell, *IEEE Trans. Ultrason., Ferroelectr., Freq. Control* **42**, 429 (1995).
- ²⁸K. N. Ying, C. Y. Ni, L. N. Dai, L. Yuan, W. W. Kan, and Z. H. Shen, *Photoacoustics* **27**, 100370 (2022).
- ²⁹M. Spies and H. Rieder, *NDT&E Int.* **43**, 425 (2010).
- ³⁰M. H. Skjelvareid, Ph.D. thesis, Faculty of Science and Technology, University of Tromsø, Norway, 2012.
- ³¹V. Perrot, M. Polichetti, F. Varray, and D. Garcia, *Ultrasonics* **111**, 106309 (2021).
- ³²J. Gazdag, *Geophysics* **43**, 1342 (1978).
- ³³C. Chen, K. N. Ying, N. Liu, L. N. Dai, W. W. Kan, and C. Y. Ni, *Chin. J. Lasers* **48**, 0304001 (2021).
- ³⁴Z. Yang, L. Peng, Z. Penghui, Z. Zhiqian, B. Xue, and M. Jian, *Chin. J. Lasers* **49**, 0909001 (2022).
- ³⁵R. E. Schramm, *Rev. Sci. Instrum.* **70**(2), 1468 (1999).
- ³⁶T. Olofsson, *IEEE Trans. Ultrason., Ferroelectr., Freq. Control* **57**, 2522 (2010).
- ³⁷J. Parra-Raad, P. Khalili, and F. Cegla, *NDT&E Int.* **111**, 102212 (2020).
- ³⁸B. Shakibi, F. Honarvar, M. D. C. Moles, J. Caldwell, and A. N. Sinclair, *NDT&E Int.* **52**, 37 (2012).